Supporting Information

Enhanced H_2O_2 Production at Reductive Potentials from Oxidized Boron-Doped Ultrananocrystalline Diamond Electrodes

James O. Thostenson[1*], Edgard Ngaboyamahina[1], Katelyn L. Sellgren[2], Brian T. Hawkins[2], Jeffrey R. Piascik[2], Ethan J. D. Klem[2], Charles B. Parker[1], Marc A. Deshusses[3], Brian R. Stoner[1,2] and Jeffrey T. Glass[1]

1 Department of Electrical and Computer Engineering, Duke University, Durham, NC

2 Research Triangle Institute (RTI) International, Research Triangle Park, NC

3 Department of Civil and Environmental Engineering, Duke University, Durham, NC

*Corresponding Author: james.thostenson@duke.edu

*__Corresponding Author__:

james.thostenson@duke.edu

H_2O_2 Absorbance-concentration curve

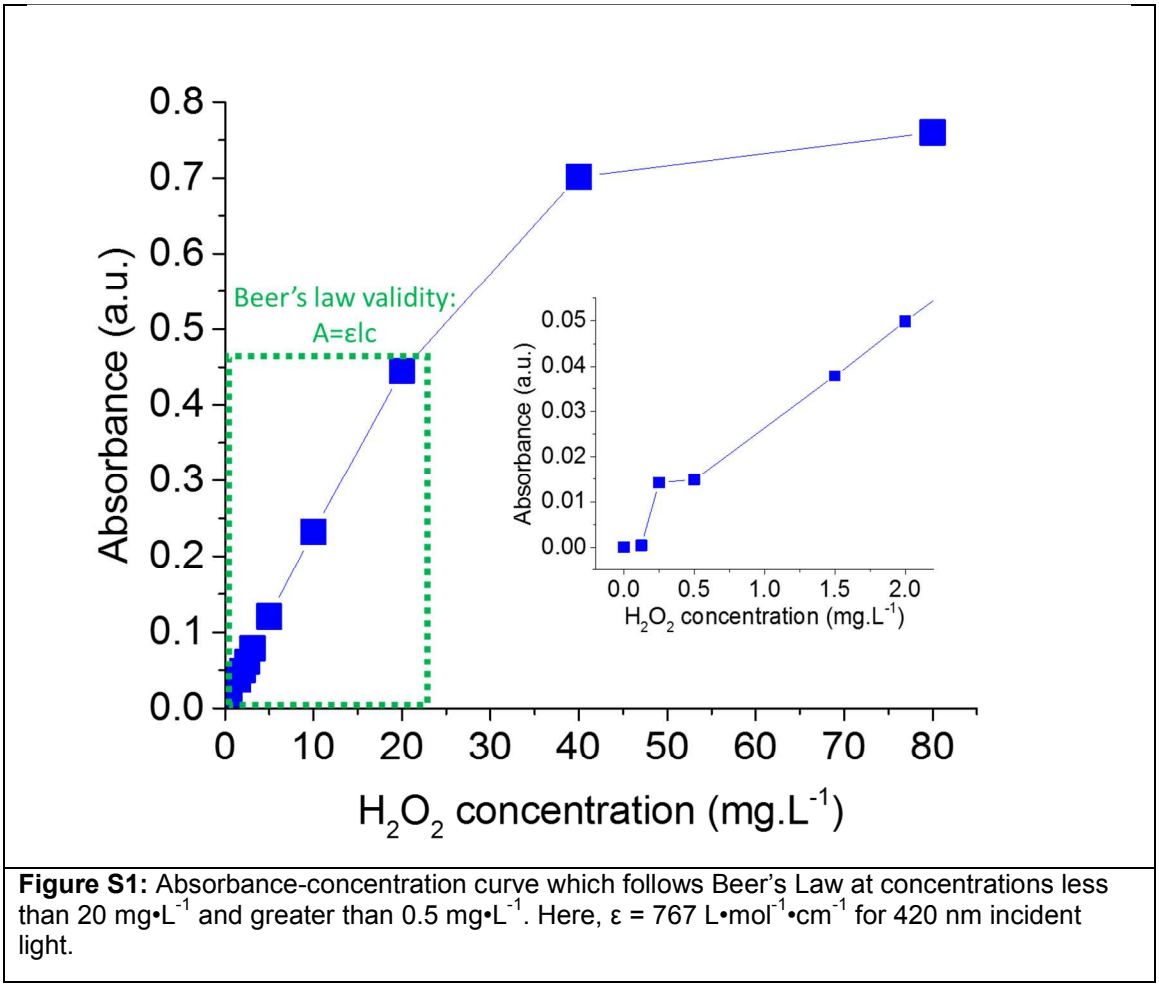

Figure S1: Absorbance-concentration curve which follows Beer's Law at concentrations less than 20 mg•L^{-1} and greater than 0.5 mg•L^{-1}. Here, ε = 767 L•mol^{-1}•cm^{-1} for 420 nm incident light.

Figure S1 is the absorbance-concentration curve generated using known concentrations of H_2O_2 in 0.12 M $Ti(SO_4)_2$. The absorbance-concentration relationship follows Beer's law when H_2O_2 concentrations, c, are 0.5 ≤ c ≤ 20 mg•L^{-1} and absorption, A, is 0.04 ≤ A ≤ 0.45. Using 420 nm light, an absorbance-coefficient, ε, of 767 L•mol^{-1}•cm^{-1} was found within the aforementioned ranges using a cuvette with an optical path-length, l, of 1 cm.

Morphology

Scanning electron microscope (SEM) images were collected using a FEI XL30 SEM-FEG. Accelerating voltages between 20-30 kV were used at a working distance between 6.6-6.8 mm, and magnification of 80 kX. Brightness and contrast of the shown 16-bit images were digitally adjusted using ImageJ at which 0.4 % of the brightest pixels were saturated at a gray-value of 65,535 to better visualize the crystallite morphology.

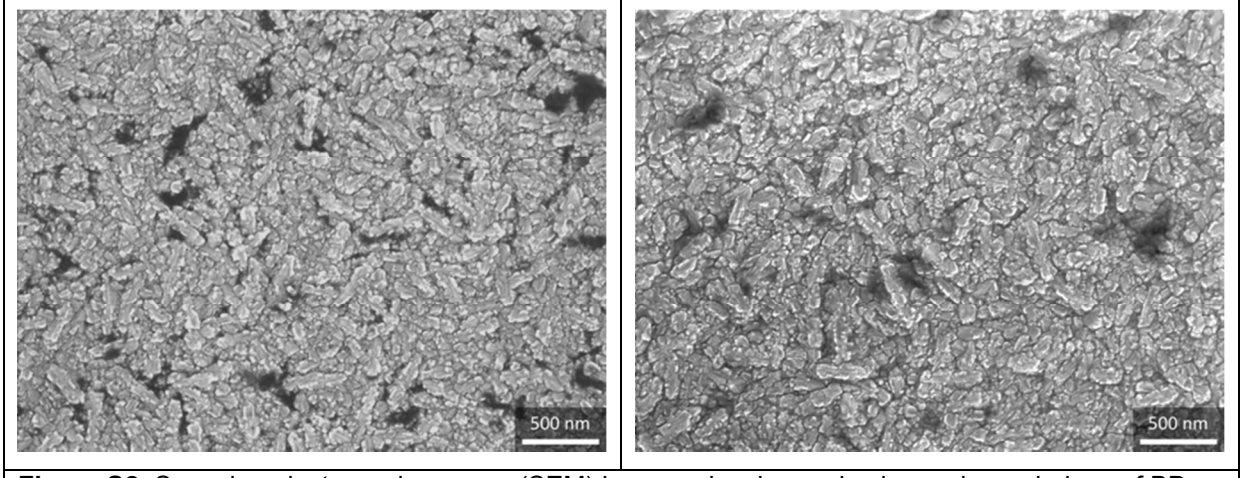

Figure S2: Scanning electron microscope (SEM) images showing grain size and morphology of BD-UNCD **A)** before and **B)** after 30 minutes of testing in 0.12 M $Ti(SO_4)_2$ at 2.5 V vs. Ag/AgCl sat. KCl

BD-UNCD possesses a high surface area, and a significant concentration of non-diamond carbon as a result of the small grain size.[1–3] Grain sizes of BD-UNCD are on the order of 3-5 nm, which equates to roughly 15 % of the grain volume existing at the surface leading to a relative increase in dangling carbon bonds, and lattice defects in comparison to MCD and NCD. The dangling bonds and lattice defects manifest as non-diamond carbon content on the surface. As a result, it has been shown that roughly 5 % of the BD-UNCD grain volume is non-diamond carbon.[4–6] Previous reports have indicated that elevated potentials (> 1.5 V vs. Ag/AgCl sat. KCl) in an aqueous acidic electrolyte can remove non-diamond carbon content at the boundaries of BDD grains, potentially altering the overall morphology of the BDD crystals.[7–9] Thus, the electrochemical studies from -2.5 to 3.5 V vs. Ag/AgCl sat. KCl presented here may etch the non-diamond carbon. However, since the removal is selective of just the small fraction of the non-diamond content on the surface (< 0.75 % of the grain volume),[1,10] the changes to the grain size, and overall morphology will be small. Figure S2 displays minimal change in the overall grain size, and morphology after 30 minutes of polarizing at 2.5 V vs. Ag/AgCl sat. KCl in 0.12 M $Ti(SO_4)_2$. Therefore, observed differences across the polarized electrodes are attributed to alterations of surface chemistry, and not gross crystallite morphology.

X-ray Photoelectron Spectroscopy Analysis of Regional Spectra

Spectra Treatment

Collected spectra were calibrated, analyzed, and deconvoluted using Casa XPS software following best practices as outlined in Briggs and Grant.[11] All data reported were the average result of 3 measurements per electrode sample. The XPS C 1s regional spectra seen in Figure S3 were normalized against the bulk peak maximum located at 285 eV, with background subtraction carried out using a Shirley background fit. Following a similar protocol as Ayers *et al.*,[12] peak assignments were made in reference to the characteristic sp^3 diamond-like-carbon C-C bonding peak located at 285 eV. For non-diamond carbon bonds, the following assignments were made: sp^2 C=C (graphitic carbon) was assigned to -1.1 eV, C-H (hydrocarbon) was assigned to +0.5 eV, C-OH (hydroxyls bonded to carbon) was assigned to +1 eV, C-O-C (ether groups) was assigned to +1.7 eV, C=O (carbonyl groups) was assigned to +3.4 eV, and COOH (carboxyl groups) was assigned to +4.1 eV. Deconvolution, and subsequent quantification of C 1s regional spectra, was carried out using Gaussian-Lorentzian peak shapes and +/- 0.2 eV constraints for FWHM and peak position, respectively, where the FWHW was set to 1eV. The resulting deconvoluted peak area quantities seen in Figure S4 were then summed to equal the relative amount of functional groups corresponding to the C-H, C-OH, C-O-C, C=O, and COOH as well as relative C=C (sp^2) content for each electrode and plotted as seen in Figure 4B. For details not mentioned herein, XPS spectra were analyzed following best practices as outlined in Briggs and Grant.[11]

	O1.5	**O2.5**	**O3.5**
Oxidation	**A** 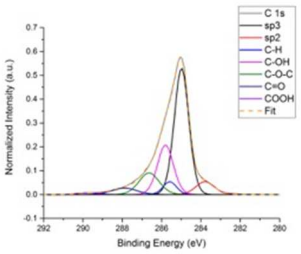	**B** 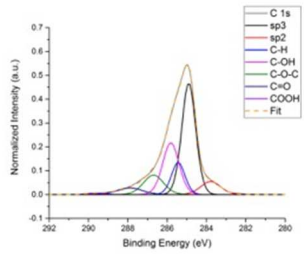	**C** 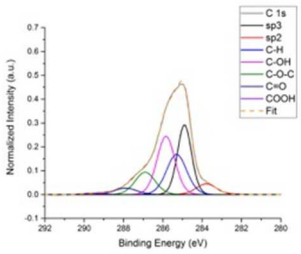
	R0.5	**R1.5**	**R2.5**
Reduction	**D** 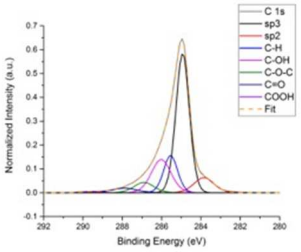	**E** 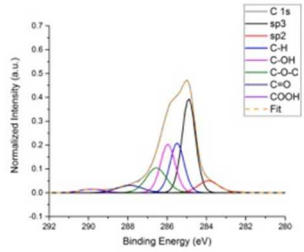	**F** 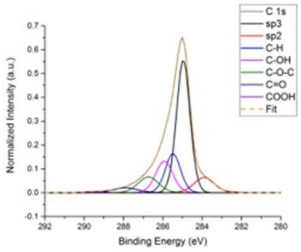
	OR1.5	**OR2.5**	**OR3.5**
Oxidation then Reduction	**G** 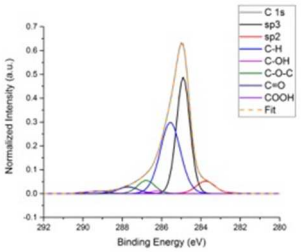	**H** 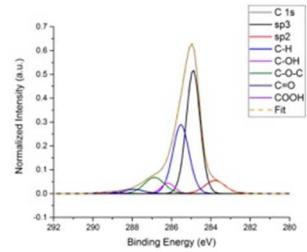	**I** 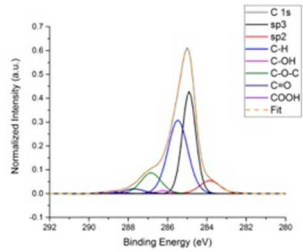

Figure S3: Deconvoluted C 1s regional spectra collected for each tested electrode in 0.12 M $Ti(SO_4)_2$, where **A-C)** correspond to the deconvoluted spectra for the O electrodes, **D-F)** correspond to the deconvoluted spectra for the R electrodes, and **G-I)** correspond to the deconvoluted spectra for the OR electrodes

R Electrodes	O Electrodes	OR Electrodes
A	**B**	**C**
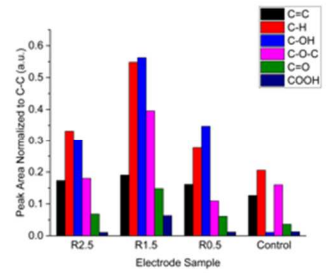	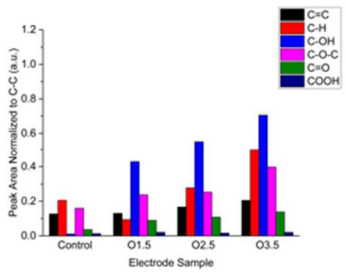	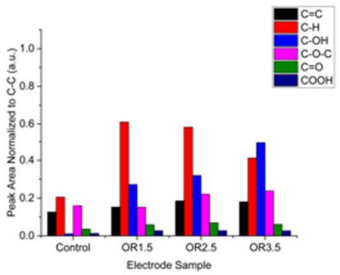
D	**E**	**F**
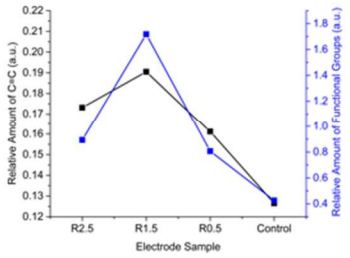	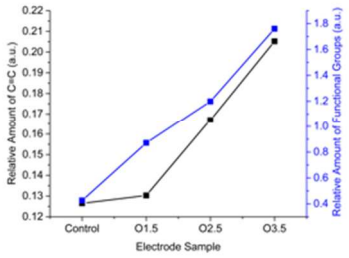	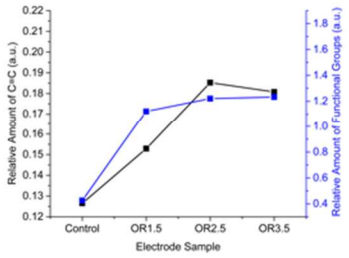

Figure S4: Deconvoluted C 1s Peak Area quantification for the **A**) R **B**) O and **C**) OR electrodes compared to the Control electrode. Integration of the C-H, C-OH, C-O-C, C=O and COOH carbon bonded functionalities for the **D**) R **E**) O and **F**) OR electrodes compared to the Control electrode

Raman Spectroscopy

Experimental

A Horiba Jobin Yvon LabRam ARAMIS Raman spectrometer with a 633 nm excitation He-Ne laser, 100 X objective was used with a 1 μm x 2 μm lateral and axial spatial resolution, respectively. Survey spectra were collected across 50-2000 cm^{-1} from which regional spectra across 1100-1600 cm^{-1} were extracted which coincide with sp^3 and sp^2 carbon bonding vibrational modes. Each spectrum was the result of 5 accumulations using a collection time of 5 s. Three spectra from each electrode sample at different spots were collected, and then averaged for use as a representative spectrum of each electrode. These spectra were then normalized against the sp^3 carbon resonant, T, peak intensity at 1296 cm^{-1}, and background subtracted by a linear fit between the spectra points at 1100 and 1600 cm^{-1}. These spectra can be seen in Figure S5. Peak assignments were made following Ferrari and Robertson. [13–15]

R Electrodes	O Electrodes	OR Electrodes

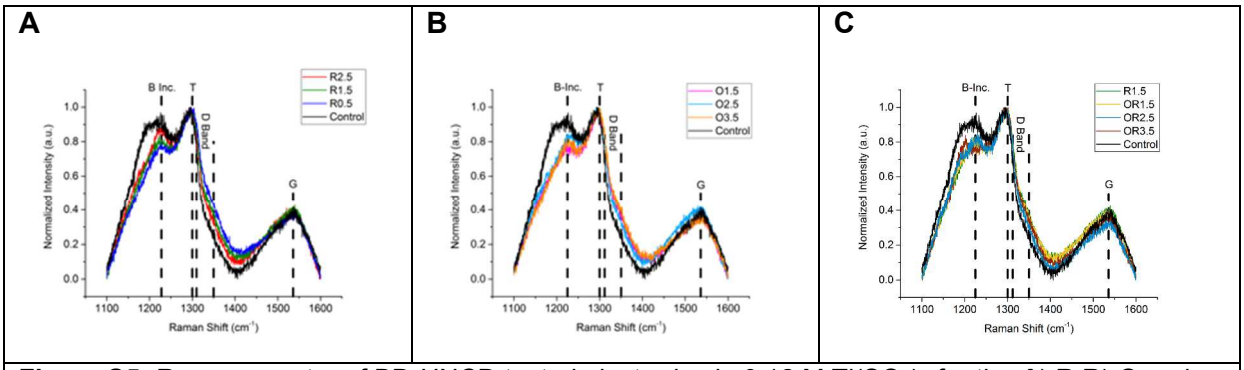

Figure S5: Raman spectra of BD-UNCD tested electrodes in 0.12 M $Ti(SO_4)_2$ for the **A**) R **B**) O and **C**) OR electrodes

Since Raman spectroscopy is largely considered a bulk characterization technique,[16] spectra shown in Figure S5A further confirm that the functional groups occur at the BD-UNCD crystallite surface. Despite the employed visible excitation wavelength (λ = 633nm) preferring sp^2 vibrational modes (G peak),[17] there is little change in the relative intensities between the T (sp^3 bonded carbon) and G peaks at 1296 and 1537 cm^{-1}, respectively. There is a slight decrease in the intensity of the peak centered at 1225 cm^{-1} which is coincident with a decreasing minima at ~1404 cm^{-1}. A similar trend was observed by Ferrari and Robertson.[15] They ascribed peaks near these wavenumbers to transpolyacetlylene segments present at grain boundaries resultant from an alteration of disordered sp^2 bonded carbon at the surface.[18] These effects tend to couple and decrease proportionally with increasing hydrogenation, similar in manner to what is illustrated in Figure S4. However, the differences are minor compared to those aforementioned and shown in the deconvoluted spectra of Figure S3-4. Thus, it is hard for one to draw conclusions as to the physical or chemical meaning of these slight trends. For BD-UNCD, the peak at 1225 cm^{-1} has been one of great discussion with some proposing that it is due to boron incorporation in the diamond lattice which causes phonon vibrational modes, while others have begun to argue that it is actually the result of perturbed diamond lattice phonons, such as disordered carbon.[19–22] When compared to the Control electrode, it appears that Raman spectra in Figure S5A indicate that even slight polarization of the BD-UNCD electrodes in the strongly acidic environment is enough to decrease this vibrational mode including a potential second peak in this region centered at ~1200 cm^{-1}. Comparison with Figure 1 seems to indicate that this decrease is correlated to the adsorption of oxygen. It is therefore possible that such adsorption corresponds to the creation of the aforementioned surface bound functional groups which are able to diminish the amount of disordered carbon at the surface, and therefore lead to a decreased intensity at 1200 cm^{-1}.

References

(1) Carlisle, J. A.; Auciello, O. Ultrananocrystalline Diamond. Properties and Applications in Biomedical Devices. *Electrochem. Soc. Interface* **2003**, *12*, 28–31.

(2) Gruen, D. M. Nanocrystalline Diamond Films. *Annu. Rev. Mater. Sci.* **1999**, *29*, 211–259. DOI: 10.1146/annurev.matsci.29.1.211.

(3) Michaelson, S.; Ternyak, O.; Hoffman, A.; Williams, O. A.; Gruen, D. M. Hydrogen Bonding at Grain Surfaces and Boundaries of Nanodiamond Films Detected by High Resolution Electron Energy Loss Spectroscopy. *Appl. Phys. Lett.* **2007**, *91*, 103104. DOI: 10.1063/1.2779848.

(4) Gruen, D. M. Ultrananocrystalline Diamond in the Laboratory and the Cosmos. *MRS Bull.* **2001**, *26*, 771–776. DOI: 10.1557/mrs2001.204.

(5) Shenderova, O. A.; Zhirnov, V. V.; Brenner, D. W. Carbon Nanostructures. *Crit. Rev. Solid State Mater. Sci.* **2002**, *27*, 227–356. DOI: 10.1080/10408430208500497.

(6) Qin, L. C.; Zhou, D.; Krauss, A. R.; Gruen, D. M. Tem Characterization of Nanodiamond Thin Films. *Nanostructured Mater.* **1998**, *10*, 649–660. DOI: 10.1016/S0965-9773(98)00092-0.

(7) Martin, H. B. Hydrogen and Oxygen Evolution on Boron-Doped Diamond Electrodes. *J. Electrochem. Soc.* **1996**, *143*, L133. DOI: 10.1149/1.1836901.

(8) Hutton, L. A.; Iacobini, J. G.; Bitziou, E.; Channon, R. B.; Newton, M. E.; Macpherson, J. V. Examination of the Factors Affecting the Electrochemical Performance of Oxygen-Terminated Polycrystalline Boron-Doped Diamond Electrodes. *Anal. Chem.* **2013**, *85*, 7230–7240. DOI: 10.1021/ac401042t.

(9) Martin, H. B. Voltammetry Studies of Single-Crystal and Polycrystalline Diamond Electrodes. *J. Electrochem. Soc.* **1999**, *146*, 2959. DOI: 10.1149/1.1392035.

(10) Williams, O. A.; Nesladek, M.; Daenen, M.; Michaelson, S.; Hoffman, A.; Osawa, E.; Haenen, K.; Jackman, R. B. Growth, Electronic Properties and Applications of Nanodiamond. *Diam. Relat. Mater.* **2008**, *17*, 1080–1088. DOI: 10.1016/j.diamond.2008.01.103.

(11) Powell, C. J.; Larson, P. E. Quantitative Surface Analysis by X-Ray Photoelectron Spectroscopy. *Appl. Surf. Sci.* **1978**, *1*, 186–201. DOI: 10.1016/0378-5963(78)90014-4.

(12) Ayres, Z. J.; Borrill, A. J.; Newland, J. C.; Newton, M. E.; Macpherson, J. V. Controlled Sp 2 Functionalization of Boron Doped Diamond as a Route for the Fabrication of Robust and Nernstian pH Electrodes. *Anal. Chem.* **2016**, *88*, 974–980. DOI:

10.1021/acs.analchem.5b03732.

(13) Ferrari, A. C.; Robertson, J. Interpretation of Raman Spectra of Disordered and Amorphous Carbon. *Phys. Rev. B* **2000**, *61*, 14095–14107. DOI: 10.1103/PhysRevB.61.14095.

(14) Ferrari, A. C.; Robertson, J. Origin of the 1150 cm−1 Raman Mode in Nanocrystalline Diamond. *Phys. Rev. B* **2001**, *63*, 121405. DOI: 10.1103/PhysRevB.63.121405.

(15) Ferrari, A. C.; Robertson, J. Resonant Raman Spectroscopy of Disordered, Amorphous, and Diamondlike Carbon. *Phys. Rev. B* **2001**, *64*, 75414. DOI: 10.1103/PhysRevB.64.075414.

(16) Ferraro, J. R.; Nakamoto, K.; Brown, C. *Introductory Raman Spectroscopy*, 2nd ed.; Elsevier, 2003.

(17) Wada, N.; Gaczi, P. J.; Solin, S. A. "Diamond-Like" 3-Fold Coordinated Amorphous Carbon. *J. Non. Cryst. Solids* **1980**, *35*, 543–548. DOI: 10.1016/0022-3093(80)90651-1.

(18) Show, Y.; Witek, M. A.; Sonthalia, P.; Swain, G. M. Characterization and Electrochemical Responsiveness of Boron-Doped Nanocrystalline Diamond Thin-Film Electrodes. *Chem. Mater.* **2003**, *15*, 879–888. DOI: 10.1021/cm020927t.

(19) Wang, S.; Swope, V. M.; Butler, J. E.; Feygelson, T.; Swain, G. M. The Structural and Electrochemical Properties of Boron-Doped Nanocrystalline Diamond Thin-Film Electrodes Grown from Ar-Rich and H2-Rich Source Gases. *Diam. Relat. Mater.* **2009**, *18*, 669–677. DOI: 10.1016/j.diamond.2008.11.033.

(20) May, P. W.; Ashfold, M. N. R.; Mankelevich, Y. A. Microcrystalline, Nanocrystalline, and Ultrananocrystalline Diamond Chemical Vapor Deposition: Experiment and Modeling of the Factors Controlling Growth Rate, Nucleation, and Crystal Size. *J. Appl. Phys.* **2007**, *101*, 53115. DOI: 10.1063/1.2696363.

(21) Tubino, R. Lattice Dynamics and Spectroscopic Properties by a Valence Force Potential of Diamondlike Crystals: C, Si, Ge, and Sn. *J. Chem. Phys.* **1972**, *56*, 1022. DOI: 10.1063/1.1677264.

(22) Turner, S.; Lu, Y. G.; Janssens, S. D.; Da Pieve, F.; Lamoen, D.; Verbeeck, J.; Haenen, K.; Wagner, P.; Van Tendeloo, G. Local Boron Environment in B-Doped Nanocrystalline Diamond Films. *Nanoscale* **2012**, *4*, 5960. DOI: 10.1039/c2nr31530k.